Transitional separation bubbles over swept wings

Nicola De Tullio

Aerodynamics and Flight Mechanics Group
University of Southampton
Southampton SO17 1BJ, UK
n.de-tullio@soton.ac.uk

Neil D. Sandham

Aerodynamics and Flight Mechanics Group
University of Southampton
Southampton SO17 1BJ, UK
n.sandham@soton.ac.uk

ABSTRACT

Direct numerical simulations and global linear stability analysis have been performed to investigate the effect of sweep on the behaviour of transitional separation bubbles developing over a NACA-0012 airfoil at moderate Reynolds numbers. The results indicate that the laminar-turbulent transition inside the bubble is greatly affected by the sweep angle, with the onset of two-dimensional vortex shedding being favoured over three-dimensional vortex shedding as sweep is increased. Both the DNS and global stability results show that the laminar-turbulent transition of the separation bubble is dominated by instability modes developing in the detached shear layer induced by the bubble and sustained by an acoustic feedback loop. An additional set of modes with relatively low frequencies and concentrated inside the separation bubble were also uncovered by a Dynamic Mode Decomposition of the DNS data. These modes are globally unstable and lead to three-dimensional oscillation of the separations bubble.

Introduction

Transitional separation bubbles (TSB) occur when the laminar flow over a solid surface separates under the influence of a sufficiently high adverse pressure gradient, generating a region of reversed flow and a highly unstable detached shear layer. The shear layer develops instabilities that drive the flow to a chaotic state and eventually cause the flow to reattach as a turbulent boundary layer. TSBs are typical of moderate Reynolds number flows over airfoils, where they exert a strong influence on aerodynamic performance. The pocket of "dead air" that forms inside the bubble limits the lift attainable, while the failure of the reattachment process leads to bubble bursts and airfoil stall.

The structure and dynamics of TSBs are greatly influenced by the underlying laminar-turbulent transition process that shapes them. A number of experiments (Dovgal *et al.*, 1994) and numerical simulations (Marxen *et al.*, 2012) have highlighted the importance of the Kelvin-Helmholtz (K-H) instability of the separated shear layer as a dominant process in TSBs. The general conclusion that arises from these investigations places emphasis on the ability of separation bubbles to strongly amplify incoming disturbances. However, self-sustained flow unsteadiness and laminar-turbulent transition in separation bubbles have been observed in various numerical investigations (see for example Pauley *et al.*, 1990; Postl *et al.*, 2011), indicating that the picture that portrays TSBs as disturbance amplifiers does not always suffice. The resonator character of TSBs has been investigated in the context of absolute and global stability analyses by a number of authors. Investigations of absolute instability in separation bubbles (Alam & Sandham, 2000; Rist & Maucher, 2002) suggest that a reversed flow of at least $15-30\%$ is needed before an absolutely unstable mode associated with the K-H instability of the separated shear layer appears. Such a mode would lead to self-sustained two-dimensional (2D) vortex shedding over which an additional self-excited three-dimensional (3D) instability may evolve (Jones *et al.*, 2008; Embacher & Fasel, 2014), driving the flow to a turbulent state. This additional mode may be viewed as an unstable global Floquet mode of the periodic flow induced by the saturated K-H instability.

Most of the research on TSBs in the past few decades has been directed towards the unswept configuration, while the effects of sweep on the TSB behaviour have received only little attention. Kaltenbach & Janke (2000) performed direct numerical simulations of transitional swept separation bubbles behind a rearward-facing step and showed that an independence principle, according to which the introduction of infinite sweep does not affect the flow characteristics in the chordwise direction, holds throughout the entire separated flow region for sweep angles up to 40°. Instability growth rates (extracted directly from the DNS data) in the detached shear layer induced by the bubble where found to grow slightly with sweep angle. The independence principle was shown to hold exactly in the case of strictly laminar swept separation bubbles by Hetsch & Rist (2009*a*), provided the free-stream velocity in the chordwise direction remains independent of sweep angle. In a follow-up study Hetsch & Rist (2009*b*) also investigated the linear stability of laminar swept separation bubbles induced over a flat plate by an adverse pressure gradient. Using local linear stability analysis (LST) and solutions of the parabolised stability equation (PSE) they showed that the linear instabilities of swept separation bubbles are not independent of sweep angle. In particular, the primary instability of the separation bubble was found to shift towards higher frequencies and spanwise wavenumbers with increasing sweep angle, while the dominant Tollmien-Schlicting wave in the attached boundary layer was only slightly affected by sweep. Despite cross-flow levels of up to 9% of the free-stream velocity, Hetsch & Rist (2009*b*) found that cross-flow instabilities played only a marginal role in the laminar-turbulent transition process, and only for the highest sweep angle of $\Lambda = 45^\circ$ analysed in their study.

The objective of the present work is to understand how sweep affects the laminar-turbulent transition process taking place on the suction side of a NACA-0012 airfoil at moderate Reynolds numbers. The investigation is carried out by performing direct numerical simulations (DNS) of the transitional flow around the airfoil at different sweep angles, complemented with global linear stability analysis.

Numerical simulations

The DNS have been carried out using the SBLI code; a highly accurate, multi-block, finite-difference solver developed at the University of Southampton. The code solves both the nonlinear and the linearised compressible Navier-Stokes equations in dimensionless form, using standard fourth-order central differences and a third-order compact Runge-Kutta method. Further details about the numerical method and validation cases can be found in De Tullio (2013) and references therein. As well as the DNS, a linearised version of the SBLI code is used in this work to solve the global eigenvalue problem around the time averaged flow fields in matrix-free, timestepper mode, with the help of the Implicitly Restarted Arnoldi

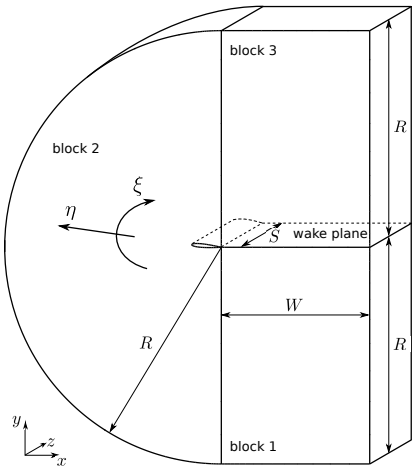

Figure 1. Sketch of the computational domain used for the direct numerical simulations.

Method provided by the parallel ARPACK library (Lehoucq *et al.*, 1997).

The numerical simulations have been performed for the flow over an infinitely swept wing with a NACA-0012 profile, modified to include a sharp trailing edge, at an incidence $\alpha = 5^\circ$, Reynolds number based on the airfoil chord $Re_c = 5 \times 10^4$ and Mach number $M = 0.4$. The investigation is carried out for two sweep angles $\Lambda = 20^\circ$ and 40°, and an un-swept wing case ($\Lambda = 0^\circ$) is also considered for comparisons. The free stream speed Q_∞ is kept constant for all the numerical simulations, regardless of the sweep angle. Hence, the velocity components in the directions perpendicular and parallel to the leading edge of the wing vary with the sweep angle according to $U_\infty = Q_\infty \cos\Lambda$ and $W_\infty = Q_\infty \sin\Lambda$, respectively. A sketch of the computational domain used for the numerical simulations is shown in figure 1. The domain is divided into three blocks, with interface boundary conditions between neighbouring blocks, and its dimensions are $R = 7.3$, $W = 5$ and $S = 0.4$ for all the simulations.

The airfoil is numerically modelled using a no-slip, isothermal boundary condition, with the wall temperature equal to the freestream temperature $T_\infty = 273.15K$. Characteristic boundary conditions are applied at all the remaining computational boundaries in order to minimise wave reflections. In particular, a zonal characteristic boundary condition Sandberg & Sandham (2006) is applied over a distance $L_{zonal} \approx 0.85c$ near the outflow boundary of blocks 1 and 3, using 61 grid points. A standard characteristic condition Thompson (1987, 1990) is applied at the rest of the boundaries, where, in addition, the freestream solution is imposed at each time step. The computational domain and grid used in this work were chosen based on those used in the work of Jones *et al.* (2008). Here, the spanwise size of the domain ($S = 0.4c$) has been doubled and the grid has also been refined in the streamwise and spanwise directions, giving a total of 567 million grid points.

A summary of the features of the computational grid employed in this study are reported in table 1. The same grid is used for all the numerical simulations. Based on the values of Δy^+_{min}, Δx^+_{max} and Δz^+_{max}, which were calculated at the position of the skin friction peak induced by the laminar-turbulent transition on the suction side of the wing, the same grid is deemed appropriate also for the swept-wing cases.

Direct numerical simulation results

A visualisation of the flow structures in the transitional flow over the suction side of the airfoil is shown in figure 2 through isosurfaces of the second invariant of the velocity gradient tensor (Q-criterion), for the three cases considered. Note that in all cases the free stream flow is from left to right. The dominant flow structures in the transitional separation bubble indicate that a K-H instability of the detached shear layer drives the initial stages of the laminar-turbulent transition process and leads to a distinct vortex shedding towards the end of the bubble. This observation agrees with previous findings reported in the literature for the unswept configuration (Jones *et al.*, 2008). Here, we further note that, while for the unswept and the $\Lambda = 20^\circ$ cases the dominant structures are three-dimensional (3D), in the $\Lambda = 40^\circ$ case vortex shedding has a stronger spanwise coherence. The initial shear layer roll up is followed by a rapid breakdown to turbulence that reattaches the flow forming a turbulent boundary layer downstream of the bubble. Note that no external disturbances have been imposed in the numerical simulations carried out in this work, so that the laminar-turbulent transition is self-sustained and cannot be attributed solely to the development of convective instabilities. The behaviour of the separation bubble clearly indicates that there are two distinct mechanisms driving the flow to a turbulent state. The first mechanism is responsible for the instability of the detached shear layer induced by the bubble and leads to a periodic vortex shedding, while the second mechanism is responsible for the rapid breakdown to turbulence that follows. In this contribution attention will be focused on the first of these two mechanisms.

A more quantitative account of the periodic vortex shedding is provided in figure 3, which shows Fourier spectra of the wall pressure perturbations at the mid-chord location, together with contours of the real part of the Fourier coefficients over the wing's suction side for the most amplified modes. In the unswept case the dominant mode of instability in the separation bubble has a structure typical of oblique-mode breakdown and is composed of two waves with Strouhal number $St \approx 5.6$ and equal and opposite spanwise wavenumbers $k_z = \pm 15.71$. This mode was not observed in Jones *et al.* (2008), who studied the same unswept wing configuration analysed here and found a dominant 2D vortex shedding for a Strouhal number (calculated using the free stream velocity and the airfoil chord) of $St = 3.37$, owing to the smaller spanwise computational domain size used in their work. For $\Lambda = 20^\circ$ vortex shedding is dominated by an oblique mode with $k_z = +15.71$ and $St \approx 6.53$. In this case, additional sub-dominant modes include a 3D mode with $k_z = -15.71$ and $St \approx 4.84$ and a 2D (i.e. parallel to the leading edge) mode with $St \approx 3.0$. For a sweep of $\Lambda = 40^\circ$ vortex shedding is excited by a broad range of 2D instability modes growing in the bubble, the most dominant of which has a frequency of $St \approx 3.0$. A peak at $St \approx 7.56$ (see blue line in figure 3) is associated with a 3D mode with $k_z = +15.71$ (note that z refers to a reference frame attached to the wing, with x being the chordwise direction).

The dominant structures in the transitional separation bubble were also investigated using Dynamic Mode Decomposition (DMD) (Schmid, 2010). In particular, here we use the streaming DMD algorithm proposed by Hemati *et al.* (2014), which allows DMD analysis to be performed in streaming mode, thereby drastically reducing the memory requirements for the computation of DMD modes. In all the three cases analysed, the DMD analysis is carried out using a $x-y$ plane placed at $z = 0.2$, combined with a $x-z$ plane placed at a distance of about 6×10^{-3} chords from the airfoil surface. The analysis is carried out over a time period of $\tau = 50$ chord-flow-through times, using snapshots of the full conservative variables vector $q = [\rho, \rho u, \rho v, \rho w, \rho E]^T$ separated by a constant time step $\Delta t = 0.05$. Figures 4(a), (b) and (c) show the DMD energy spectra, together with contours of the real part of the u-velocity mode functions for two of the most energetic modes for cases S0, S20 and S40, respectively. Note that mode energies were

Case	R/c	W/c	S/c	N_{foil}	N_{wake}	N_ξ	N_η	N_z	Δy^+_{min}	Δx^+_{max}	Δz^+_{max}
S0	7.3	5.0	0.4	1799	1602	3401	692	240	0.92	3.46	4.92
Jones *et al.* (2008)	7.3	5.0	0.2	1066	1506	2570	692	96	1.0	3.36	6.49
S20	7.3	5.0	0.4	1799	1602	3401	692	240	0.92	3.45	4.92
S40	7.3	5.0	0.4	1799	1602	3401	692	240	0.92	3.43	4.97

Table 1. Details of the computational study.

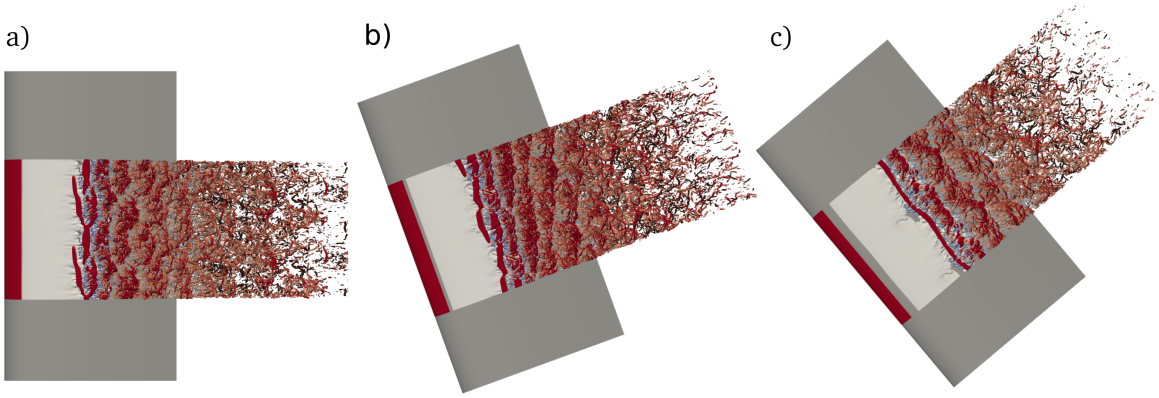

Figure 2. Flow structures in the transitional separation bubble, shown through isosurfaces of Q-criterion coloured by streamwise velocity contours (top view). The white isosurfaces show regions of reversed flow. The flow is from left to right. a) case S0, b) case S20 and c) case S40.

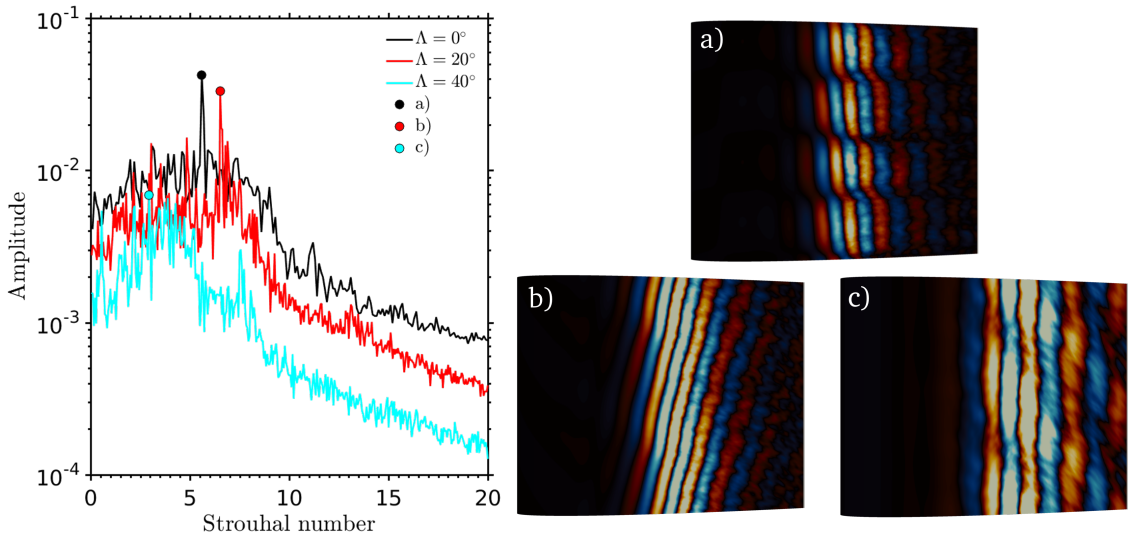

Figure 3. Wall pressure Fourier analysis. Span-averaged Fourier coefficient amplitudes at mid chord and contours of the real part of the wall pressure Fourier coefficients showing the structure of the dominant modes during breakdown to turbulence. a) Unswept, b) 20 degrees sweep and c) 40 degrees sweep

scaled with the energy of the mean flow mode (the most energetic mode), seen in the spectra of figure 4 at $St = 0$ and unit energy. While some of the DMD modes extracted correspond to dynamical features of the turbulent boundary layer, the analysis here is focused on the modes that relate to the separation bubble transition process. For case S0 in figure 4(a) one of the dominant DMD modes occurs for a Strouhal number of $St = 5.56$. This mode is the dominant instability identified by the Fourier analysis and, as suggested by the associated eigenfunction, is the manifestation of an oblique K-H instability of the detached shear layer placed above the bubble. Two-dimensional linear instabilities also play an important role in the laminar-turbulent transition of the separation bubble in this case. The dominant 2D DMD mode in this case is shown in 4(a); it is also of K-H type and has a frequency $St = 4.0$. Case S20, shown in figure 4(b), has a distinct peak in the DMD energy spectrum at $St = 6.66$, which again corresponds with the dominant instability mode identified in the Fourier analysis. The DMD eigenfunction indicates that this mode is an oblique K-H instability of the detached shear layer

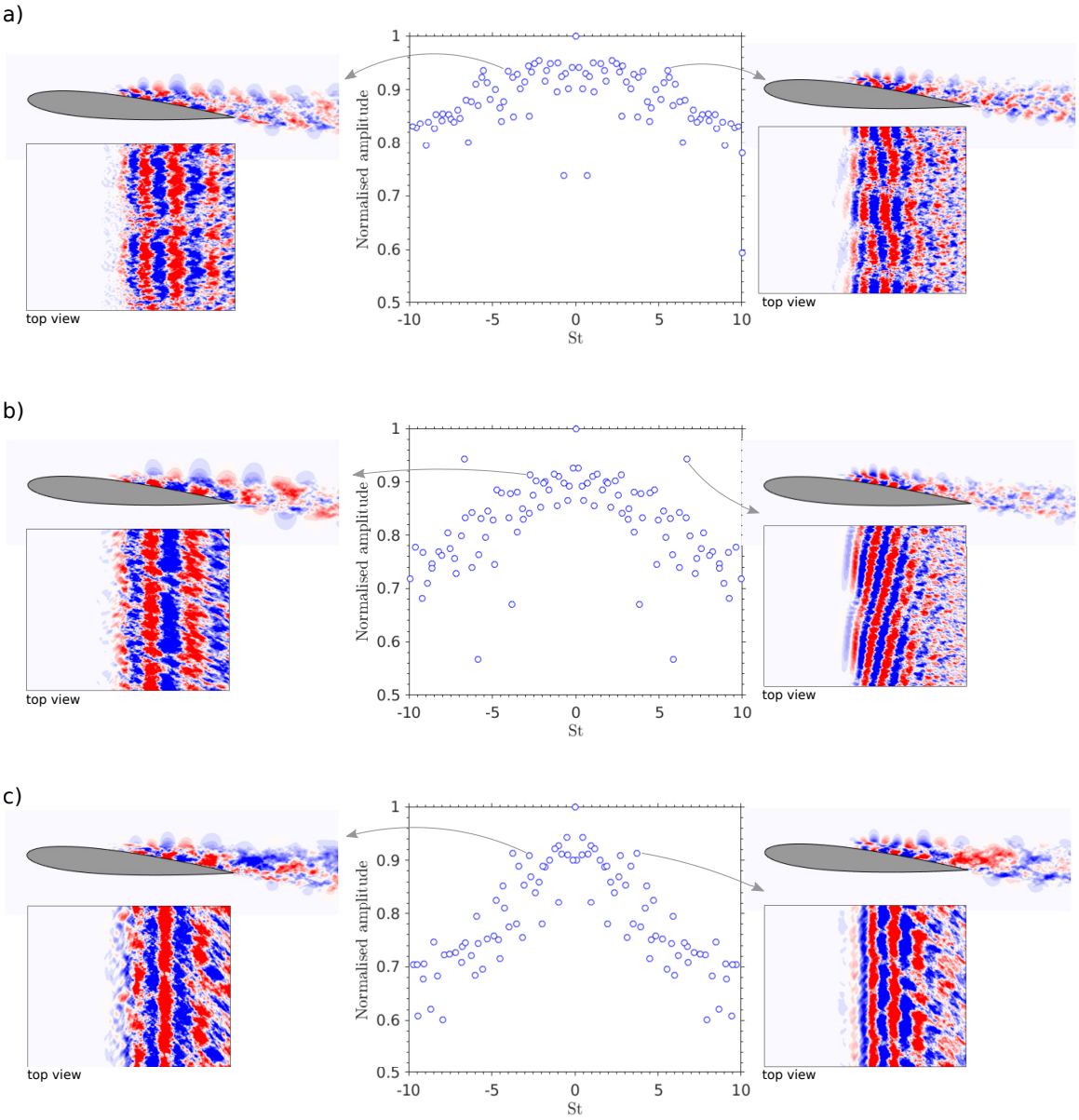

Figure 4. Dynamic mode decomposition spectra and contours of the real part of the u-velocity for some of the most energetic DMD modes. a) case S), b) case S20 and c) case S40.

above the bubble, travelling in the positive spanwise direction. Two-dimensional modes also take part in the laminar-turbulent transition process in this case, the most amplified of which is shown in figure 4(b) and has a frequency of $St = 2.74$. The dominant K-H modes are all 2D for case S40. Figure 4(c) shows that the S40 DMD spectrum has a peak at around $St = 3.0$ and the most dominant modes extracted from the DNS results have $St = 2.7$ (left) and $St = 3.7$ (right) and are both manifestations of a 2D K-H instability of the detached shear layer.

It is interesting to note that, while for the unswept case the wave vectors of the 3D modes developing in the bubble do not have a preferred orientation in the spanwise direction, the dominant 3D modes found in the swept cases always have a preferred orientation, which is dependent on the frequency of the mode. There may be different factors causing this behaviour. Instabilities will exhibit different spatial growth rates when travelling in the positive or negative spanwise direction when a nonzero mean spanwise velocity is present in the flow. Another important factor has to do with the receptivity of the convectively unstable modes. In a reference frame xyz with nonzero u_z velocity, the dispersion relation for an acoustic wave is not symmetric about $k_z = 0$, hence, for a fixed frequency, the chordwise wavenumber (k_x) for an acoustic wave travelling backwards against the flow is different for positive and negative k_z. This can be shown by writing the dispersion relation for a neutral, plane acoustic wave in the free-stream in the xyz reference frame (i.e. the reference frame used in the numerical simulations), which takes the form

$$St = \frac{|\mathbf{k}|}{2\pi}\left[\cos(\Lambda - \theta) + M^{-1}\right], \tag{1}$$

where $|\mathbf{k}| = \sqrt{k_x^2 + k_z^2}$, $\theta = \arctan(k_z/k_x)$ is the propagation angle in the $x-z$ plane and the sweep angle Λ is also the angle between the x direction and the free-stream flow direction. Figure 5 shows the variation of St against k_x for $k_z = 0$ and $k_z = \pm 15.71$, which is the minimum nonzero spanwise wavenumber contained in the computational domain. While for the unswept case the dispersion relation is symmetric about k_z, as already anticipated the dispersion rela-

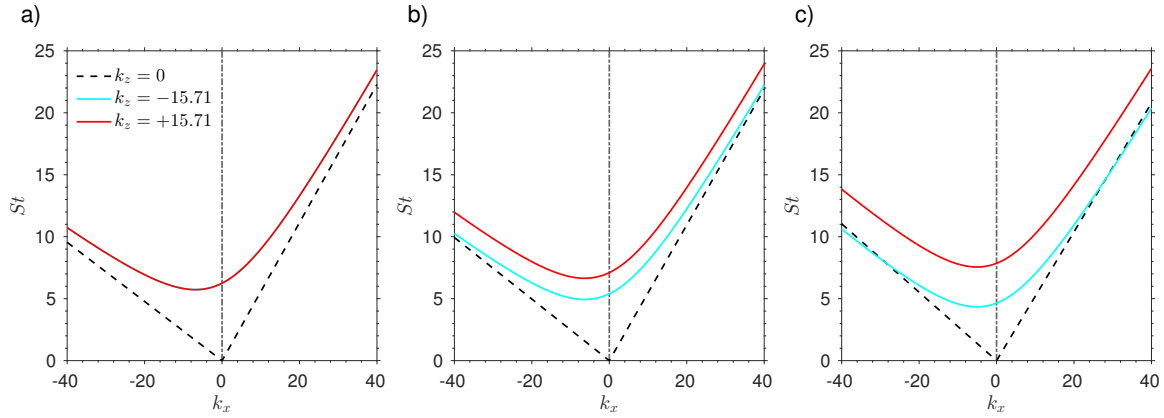

Figure 5. Dispersion relations for oblique acoustic waves. a) case S0, b) case S20 and c) case S40.

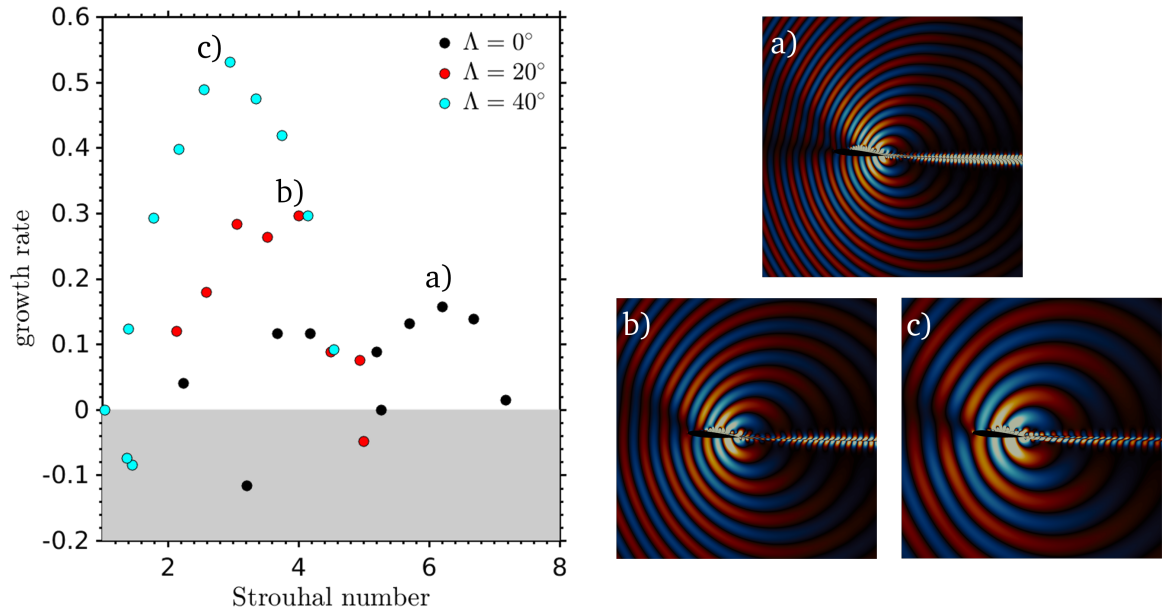

Figure 6. Global 2D spectra. The eigenfunctions of the most unstable modes are shown in the insets through contours of the real part of the velocity divergence field. a) case S0, b) case S20 and c) case S40.

tions for $k_z > 0$ and $k_z < 0$ differ in the case of nonzero sweep. For example at $St = 7.56$ in the $\Lambda = 40°$ case, the chordwise wavenumbers for $k_z = +15.71$ are $k_x = -4.49$ and $k_x = -5.63$, while for $k_z = -15.71$ we have $k_x = -27.15$ and $k_x = 11.55$. Such a large difference in the wavenumbers of the acoustic waves travelling backwards against the flow, in turn, affects the receptivity of boundary layer instabilities due to the interaction between the acoustic waves and the airfoil's leading edge.

In order to further investigate the origin of the self-sustained vortex shedding, a global linear stability analysis of the time- and span-averaged flow fields was performed. Figure 6 shows the 2D ($k_z = 0$) global spectra for the different degrees of sweep, together with the eigenfunctions of the most unstable modes in each case. The mean flows obtained for the different sweep angles are able to sustain the growth of 2D globally unstable modes. The spectrum appears to be formed by two different branches for case S0. The first branch is centred at about $St = 4.0$ and the second at about $St = 6.0$. While the peak growth rate for the first branch agrees well with the frequency of the most amplified 2D DMD mode for case S0, the second branch was not found in the DMD or Fourier analyses. One possible explanation for this discrepancy may be that the frequency range of the second 2D branch overlaps with that of the dominant (3D) instability for this case. For case S20, the most unstable 2D global modes occur for frequencies in the range $St = 3.0 - 4.0$. The agreement between global linear stability and DMD and Fourier analyses is reasonable in this case, with the dominant 2D DMD and Fourier modes found for frequencies $St = 2.74$ and $St = 3.0$, respectively. For case S40 a single branch of highly unstable modes can be observed, centred at $St = 3.0$. This is in very good agreement with the DNS data; the dominant DMD and Fourier modes were found for frequencies between $St = 2.7$ and $St = 3.7$, and for $St = 3.0$, respectively. As shown by the eigenfunctions in figure 6, all the unstable modes are characterised by a strong acoustic feedback (originating at the airfoil's trailing edge) that feeds the convective instability of the detached shear layer and drives the global instability of the flow. The growth rate of the most unstable 2D global modes increases with increasing sweep angle, with the most unstable mode for $\Lambda = 40°$ growing almost twice as fast as its $\Lambda = 20°$ counterpart.

In addition to the self-sustained K-H modes that lead to the characteristic vortex shedding shown in figure 2, a different kind of mode, characterised by a relatively low oscillation frequency and principal support inside the separation bubble, was also uncovered by the DMD analysis. Figure 7(a) and (b) show the eigenfunctions of the leading low frequency modes for cases S20 and S40, respectively. They have a frequency of $St = 0.18$ for case S20 and $St = 0.5$

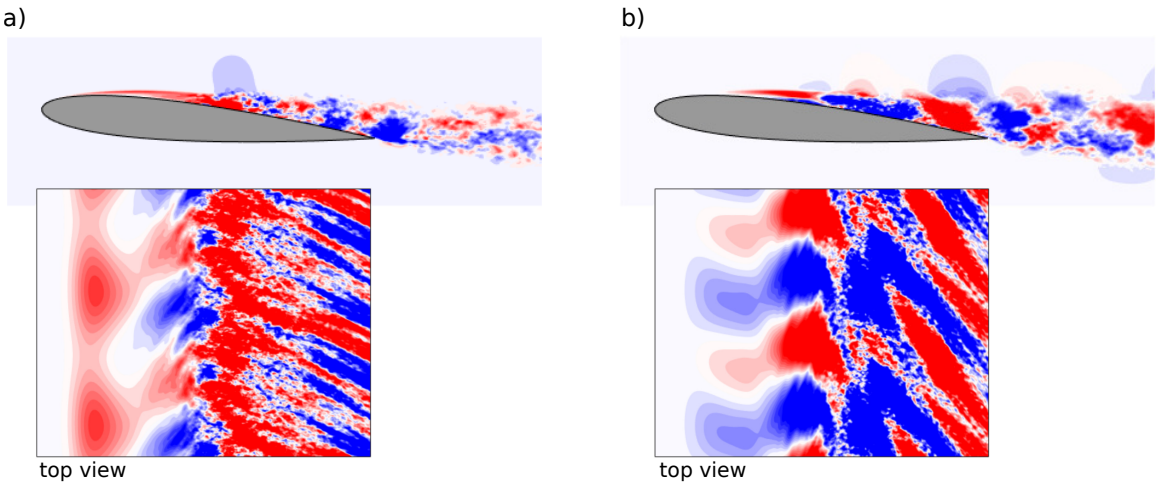

Figure 7. Low frequency bubble DMD modes, shown through contours of the real part of the u-velocity eigenfunction. a) case S20, $St = 0.18$ and b) case S40, $St = 0.5$.

for case S40 and can be identified in the DMD spectra in figures 4(b) and (c), respectively, as the most energetic modes near $St = 0$. These modes are associated with three-dimensional global oscillations of the separation bubble and appear to play a primary role in the laminar-turbulent transition process inside the bubble. This is especially true for the cases with sweep, although a low frequency mode also exists in the unswept case, as can be seen in the DMD spectrum in 4(a) near $St = 0$. In particular, for case S40 the $St = 0.5$ mode is responsible for the slight spanwise modulation of the 2D vortex visible in figure 2(c) near the back of the bubble.

Conclusions

Direct numerical simulations and global stability analysis were carried out to investigate the effect of sweep on the dynamics of the transitional separation bubbles forming on the suction side of a NACA-0012 airfoil. The results show that the laminar-turbulent transition of the separation bubbles leads to the shedding of vortices at the back of the bubble, which is caused by the spatial growth of a K-H instability of the detached shear layer induced by the bubble. The convective instability of the shear layer is sustained by an acoustic feedback loop originating at the airfoil's trailing edge. Sweep affects this self sustained transition process mainly by modifying the dispersion relation of the acoustic waves responsible for the excitation of the instability modes, leading to different characteristics of the dominant shear layer modes for different angles of sweep. In all the cases analysed, the separation bubble was found to undergo three-dimensional oscillations due to the existence of a globally unstable mode, with frequencies about one order of magnitude lower than the dominant shear layer mode. The results from a global two-dimensional linear stability study were found to be in good agreement with the DNS data.

REFERENCES

Alam, M. & Sandham, N. D. 2000 Direct numerical simulation of short laminar separation bubbles with turbulent reattachment. *J. Fluid Mech.* **410**, 1–28.

De Tullio, N. 2013 Receptivity and transtion to turbulence of supersonic boundary layers with surface roughness. PhD thesis, University of Southampton, Southampton, UK.

Dovgal, A. V., Kozlov, V. V. & Michalke, A. 1994 Laminar boundary layer separation: instability and associated phenomena. *Prog. Aero. Sciences* **3**, 61–94.

Embacher, M. & Fasel, H. F. 2014 Direct numerical simulations of laminar separation bubbles: investigation of absolute instability and active flow control of transition to turbulence. *J. Fluid Mech.* **747**, 141–185.

Hemati, M. S., Williams, M. O. & Rowley, C. W. 2014 Dynamic mode decomposition for large and streaming datasets. *Physics of Fluids* **26** (111701).

Hetsch, T. & Rist, U. 2009*a* An analysis of the structure of laminar separation bubbles in swept infinite geometries. *Eur. J. Mech. B/Fluids* **28** (4), 486–493.

Hetsch, T. & Rist, U. 2009*b* The influence of sweep on the linear stability of a series of swept laminar separation bubbles. *Eur. J. Mech. B/Fluids* **28** (4), 494–505.

Jones, L. E, Sandberg, R. D. & Sandham, N. D. 2008 Direct numerical simulations of forced and unforced separation bubbles on an airfoil at incidence. *J. Fluid Mech.* **602**, 175–207.

Kaltenbach, H.-J. & Janke, G. 2000 Direct numerical simulation of flow separation behind a swept, rearward-facing stepat $Re_H = 3000$. *Physics of Fluids* **12** (9), 2320–2337.

Lehoucq, R., Sorensen, D. & Yang, C. 1997 Arpack users' guide: Solution of large scale eigenvalue problems with implicitly restarted Arnoldi methods.

Marxen, O., Lang, M. & Rist, U. 2012 Discrete linear local eigenmodes in a separating laminar boundary layer. *J. Fluid Mech.* **711**, 1–26.

Pauley, L. L., Moin, P. & Reynolds, W. C. 1990 The structure of two-dimensional separation. *J. Fluid Mech.* **220**, 397–411.

Postl, D., Balzer, W. & Fasel, H. F. 2011 Control of laminar separation using pulsed vortex generator jets: direct numerical simulations. *J. Fluid Mech.* **676**, 81–109.

Rist, U. & Maucher, U. 2002 Investigations of time-growing instabilities in laminar separation bubbles. *Eur. J. Mech. B/Fluids* **21**, 495–509.

Sandberg, R.D. & Sandham, N.D. 2006 Nonreflecting zonal characteristic boundary condition for direct numerical simulation of aerodynamic sound. *AIAA J.* **44** (2), 402–405.

Schmid, P. J. 2010 Dynamic mode decomposition of numerical and experimental data. *J. Fluid Mech.* **656**, 5–28.

Thompson, K. W. 1987 Time dependent boundary conditions for hyperbolic systems. *Journal of Computational Physics* **68**, 1–24.

Thompson, K. W. 1990 Time dependent boundary conditions for hyperbolic systems, II. *Journal of Computational Physics* **89**, 439–461.